Quaternary Science Reviews 181 (2018) 65–75

Contents lists available at ScienceDirect

Quaternary Science Reviews

journal homepage: www.elsevier.com/locate/quascirev

Constraining Quaternary ice covers and erosion rates using cosmogenic $^{26}Al/^{10}Be$ nuclide concentrations

Mads Faurschou Knudsen*, David Lundbek Egholm

Department of Geoscience, Aarhus University, Høegh-Guldbergs Gade 2, DK-8000, Aarhus C, Denmark

ARTICLE INFO

Article history:
Received 5 May 2017
Received in revised form
5 September 2017
Accepted 7 December 2017
Available online 12 December 2017

Keywords:
Cosmogenic nuclides
$^{26}Al/^{10}Be$ ratios
Monte Carlo modelling
Variable erosion rates
Glacial plucking
Ice-cover history
Quaternary

ABSTRACT

Paired cosmogenic nuclides are often used to constrain the exposure/burial history of landforms repeatedly covered by ice during the Quaternary, including tors, high-elevation surfaces, and steep alpine summits in the circum-Arctic regions. The approach generally exploits the different production rates and half-lives of ^{10}Be and ^{26}Al to infer past exposure/burial histories. However, the two-stage minimum-limiting exposure and burial model regularly used to interpret the nuclides ignores the effect of variable erosion rates, which potentially may bias the interpretation. In this study, we use a Monte Carlo model approach to investigate systematically how the exposure/burial and erosion history, including variable erosion and the timing of erosion events, influence concentrations of ^{10}Be and ^{26}Al. The results show that low $^{26}Al/^{10}Be$ ratios are not uniquely associated with prolonged burial under ice, but may as well reflect ice covers that were limited to the coldest part of the late Pleistocene combined with recent exhumation of the sample, e.g. due to glacial plucking during the last glacial period. As an example, we simulate published $^{26}Al/^{10}Be$ data from Svalbard and show that it is possible that the steep alpine summits experienced ice-free conditions during large parts of the late Pleistocene and varying amounts of glacial erosion. This scenario, which contrasts with the original interpretation of more-or-less continuous burial under non-erosive ice over the last ~1 Myr, thus challenge the conventional interpretation of such data. On the other hand, high $^{26}Al/^{10}Be$ ratios do not necessarily reflect limited burial under ice, which is the common interpretation of high ratios. In fact, high $^{26}Al/^{10}Be$ ratios may also reflect extensive burial under ice, combined with a change from burial under erosive ice, which brought the sample close to the surface, to burial under non-erosive ice at some point during the mid-Pleistocene. Importantly, by allowing for variable erosion rates, the model results may reconcile spatially varying $^{26}Al/^{10}Be$ data from bedrock surfaces preserved over multiple glacial cycles, suggesting that samples from the same high-elevation surface or neighbouring alpine summits may have experienced similar long-term burial under ice, but varying amounts of glacial erosion.

1. Introduction

The extent and longevity of past and present ice sheets represent topics of wide interest, because they are key to understand how ice sheets respond to climatic changes, and, in turn, influence global sea level (Lambeck et al., 2014; Clark et al., 2016, Schaefer et al., 2016; Bierman et al., 2016; Blard and Leduc, 2016; Glasser, 2016). They are also important because ice sheets and cold-climate processes have shaped much of the landscape we observe at high latitudes and in mountainous regions today (Sugden, 1974; Sugden and John, 1976; Kessler et al., 2008). It is inherently difficult, however, to study the extent and longevity of past glaciations, as the geological evidence remains fragmentary (Nielsen and Kuijpers, 2013). The terrestrial deposits that bear witness of past glacial-interglacial cycles are often removed by subsequent glacial advances (Gibbons et al., 1984), and it is therefore difficult to establish past ice-sheet variations pre-dating the Last Glacial Maximum (LGM) around 21 kyr ago, except when the ice advanced beyond the LGM limit. In the absence of geological evidence, many studies rely on measurements of paired cosmogenic radionuclides in bedrock samples. This approach exploits the fact that the cosmogenic nuclides ^{10}Be and ^{26}Al are produced at known rates and at a fixed ratio of ~6.75 (Nishiizumi et al., 1989; Balco et al., 2008), although recent studies suggest this production ratio may be higher (Argento et al.,

* Corresponding author.
E-mail address: mfk@geo.au.dk (M.F. Knudsen).

https://doi.org/10.1016/j.quascirev.2017.12.012

2013; Corbett et al., 2017) and vary with latitude and altitude (Argento et al., 2015a, 2015b; Borchers et al., 2016). The ratio in a sample, however, changes over time, both under continuous exposure with steady erosion and when buried under ice or rock, because the two nuclides have different half-lives. Since the mid-1980's, ratios of $^{26}Al/^{10}Be$ have been used to study the long-term exposure/burial and erosion history of non-glaciated areas, such as the Libyan desert (Klein et al., 1986), and subsequently in glaciated areas such as Antarctica (Nishiizumi et al., 1991). This research initiated the use of the two-stage $^{26}Al/^{10}Be$ vs. ^{10}Be diagram to either infer mean erosion rates for the limiting case of steady-state surface exposure, or minimum-limiting exposure and burial durations for the limiting case of no erosion (Nishiizumi et al., 1991; Granger, 2006). The minimum-limiting exposure and burial durations represent the simplest and shortest possible exposure/burial history that can explain concentrations of ^{10}Be and ^{26}Al measured in rock samples (Fig. 1). In this model, samples plotting along a burial isochron is interpreted to have experienced equal lengths of burial irrespective of the absolute ^{10}Be concentration.

Paired $^{26}Al/^{10}Be$ data from bedrock surfaces have been used to study the landscape history and past glacial ice cover in areas that were covered by ice during parts of the Quaternary, including Svalbard (Gjermundsen et al., 2015), Minnesota in the US (Bierman et al., 1999), the Torngat Mountains (Staiger et al., 2005) and Baffin Island in arctic Canada (Briner et al., 2006, 2014; Margreth et al., 2016), as well as several areas in western Greenland (Roberts et al., 2009, 2013; Lane et al., 2014; Corbett et al., 2013; Beel et al., 2016). Low $^{26}Al/^{10}Be$ ratios have been used to infer prolonged periods of burial under cold-based ice in several of these areas (e.g. Bierman et al., 1999; Briner et al., 2006; Corbett et al., 2013; Gjermundsen et al., 2015), whereas high $^{26}Al/^{10}Be$ ratios have been used to infer limited burial under ice (e.g. Beel et al., 2016; Strunk et al., 2017). Examples include high-elevation surfaces in western Greenland and the steep alpine summits of Svalbard that were interpreted by the authors as largely buried under cold-based, non-erosive ice throughout the latter half of the Quaternary (Corbett et al., 2013; Gjermundsen et al., 2015). In contrast, other studies of paired $^{26}Al/^{10}Be$ bedrock data from western Greenland indicate that burial under ice during the Quaternary was very limited, suggesting that some of the high-elevation surfaces around Uummannaq may have remained as nunataks during the most recent glacial maxima (Beel et al., 2016). The ice-cover history inferred for the Ummannaq area is thus very different than the history inferred for other areas in western Greenland. In general, it may be difficult to reconcile ice-cover histories based on spatially varying $^{26}Al/^{10}Be$ ratios, because it requires regionally, and in some cases locally, varying long-term ice-covers. Such discrepancies are highlighted by the fact that samples from the same area, or even the same sample site (e.g. Gjermundsen et al., 2015), frequently show significantly different $^{26}Al/^{10}Be$ ratios.

The discrepancies highlighted above reveal some fundamental difficulties concerning the use of the two-isotope $^{26}Al/^{10}Be$ vs. diagram to constrain complex burial histories. First of all, the $^{26}Al/^{10}Be$ vs. ^{10}Be burial concept generally assumes constant erosion rates (Nishiizumi et al., 1991). For example, exhumation of a rock sample at a steady pace of 1 m/Myr under ice-free conditions (from a depth of 2.6 m–0 m during the Quaternary) leads to ^{10}Be and ^{26}Al concentrations that correctly indicates zero ice cover in the $^{26}Al/^{10}Be$ vs. ^{10}Be burial plot (black line in Fig. 2). However, as pointed out by Gosse & Phillips (2001) and discussed by others (e.g. Small et al., 1997; Bierman et al., 1999), the resulting point is shifted significantly within the $^{26}Al/^{10}Be$ vs. ^{10}Be diagram if the same amount of erosion (2.6 m) is episodic, or occurs at accelerating/decelerating erosion rates (blue and green lines in Fig. 2). An accelerating rate of erosion may thus falsely indicate long-term burial under ice, even when the erosion occurs under fully ice-free conditions (blue lines in Fig. 2). Secondly, the nuclide inventory at the onset of the Quaternary may be non-negligible if the pre-Quaternary erosion rate and the total erosion during the Quaternary was low, which further complicates the use of the $^{26}Al/^{10}Be$ vs. ^{10}Be diagram.

In this study, we introduce a novel Monte Carlo model that fully integrates the effects of both constant and variable erosion as well as pre-Quaternary inheritance in a systematic effort to map how different exposure/burial and erosion histories influence the resulting ^{10}Be and ^{26}Al concentrations. We show that variable erosion rates, including the timing of the erosion, may critically influence the concentrations of ^{10}Be and ^{26}Al that we measure in rock samples. These effects challenge the conventional interpretation of paired $^{26}Al/^{10}Be$ data from areas covered by ice during the Quaternary.

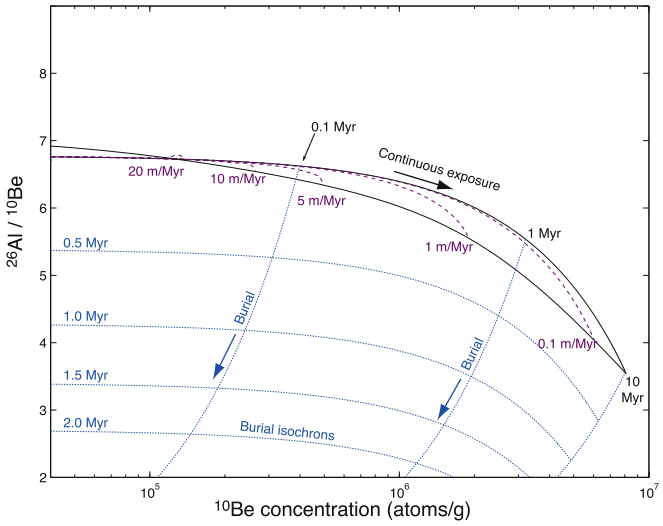

Fig. 1. Standard $^{26}Al/^{10}Be$ vs. ^{10}Be diagram used to interpret paired $^{26}Al/^{10}Be$ data from bedrock surfaces with the minimum-limiting exposure and burial model. Lines in the $^{26}Al/^{10}Be$ vs. ^{10}Be diagram, including burial isochrons, are calculated using the production rates, half-lives, and attenuations lengths reported in Margreth et al. (2016).

2. Simulating ^{10}Be-^{26}Al concentrations using a Monte Carlo approach

The model framework used in this study to simulate the evolution of terrestrial cosmogenic nuclide (TCN) concentrations over multiple glacial-interglacial cycles during the Quaternary combines key aspects of the approaches by Knudsen et al. (2015) and Margreth et al. (2016), although with some important differences. Similar to Knudsen et al. (2015), we use a Lagrangian approach that tracks the depth of a sample as it moves towards the surface due to erosion. The exposure/burial history associated with climatic changes and advancing/retreating ice sheets during the Quaternary is determined by applying a threshold value (Kleman et al., 2008; Fabel et al., 2002; Knudsen et al., 2015) to the global benthic marine $\delta^{18}O$ record (Lisiecki and Raymo, 2005), which is a proxy for past global land-ice volume. The $\delta^{18}O$-threshold value is randomly selected from a linear interval (3.25–4.85‰) with uniform probability. With this approach, we assume that the exposure/burial history can be divided into two distinct regimes: i) glacial periods with negligible or no exposure due to overlying ice, and ii) interglacial periods characterized by full exposure (Fig. 3), hereby assuming that shielding due to snow, till, or vegetation is negligible. Interglacial periods are furthermore characterized by a constant

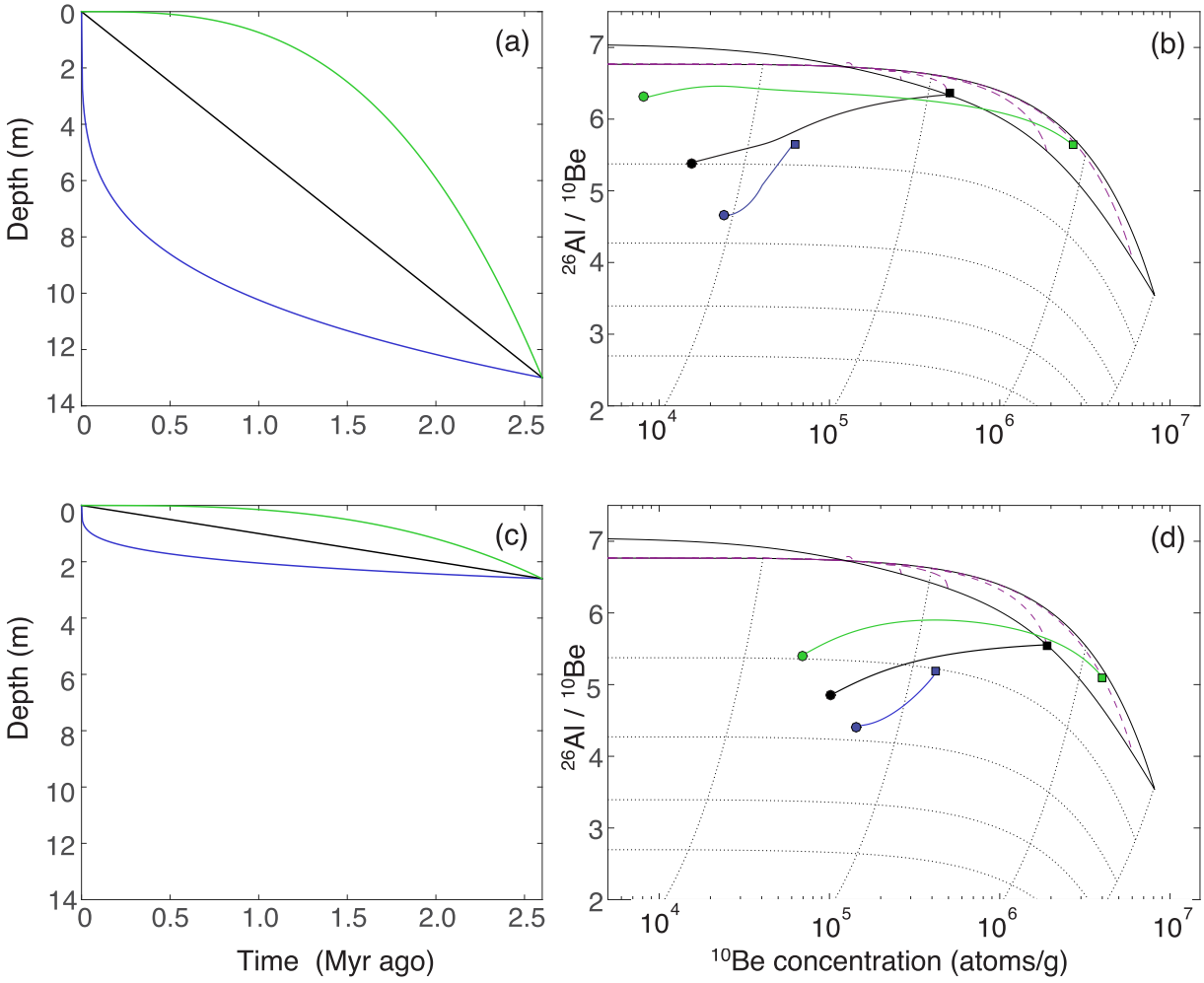

Fig. 2. Theoretical exhumation histories for synthetic samples that experienced a total of (a) 13 m and (c) 2.6 m of subaerial erosion in a non-glacial setting during the Quaternary. None of the synthetic samples experienced any shielding due to overlying ice. Panels (b) and (d) show the ^{26}Al/^{10}Be vs. ^{10}Be trajectories in the two-isotope diagram associated with the theoretical exhumation histories in panel (a) and (c), respectively. Circles denote starting points associated with the onset of the Quaternary (for different pre-Quaternary erosion rates defined by the gradient at the onset of the Quaternary 2.6 Myr ago), whereas squares denote end points associated with the present. Blue colours denote exhumation histories characterized by accelerating erosion rates during the Quaternary, while green colours denote decelerating erosion rates during the Quaternary. Black colours denote constant erosion rates during the Quaternary. Note how the shape of the exhumation histories determines the end point in the burial plot. (For interpretation of the references to colour in this figure legend, the reader is referred to the Web version of this article.)

subaerial erosion rate that is randomly selected from a logarithmic interval (0.05–50 m/Myr) with uniform probability. The interval thus spans scenarios with very low subaerial erosion rates, such as burial of bedrock under regolith, to scenarios with much more efficient subaerial erosion. The primary focus of this study is on scenarios with low subaerial erosion rates, because higher rates imply a decrease in the amount of inheritance. This renders the higher rates increasingly irrelevant to the focus of our study.

In this study, glacial erosion is not simulated as a constant rate of mass removal from the surface, as in Knudsen et al. (2015) and Strunk et al. (2017), but rather as distinct erosion events akin to the approach of Margreth et al. (2016). Every glacial period thus experiences an erosion event, in which removal of material from the surface simulates bedrock abrasion and plucking, or stripping of regolith that may have developed through interglacial bedrock weathering (e.g. Anderson and Anderson, 2010). The thickness of the material removed in each glacial period, which is independent of erosion during previous glacial periods, is selected randomly from a logarithmic interval with uniform probability. However, to ensure that a wide range of possible model-parameter combinations, which represent various geologically plausible exposure/burial and erosion histories, are thoroughly explored, we combine different probability distributions to cover the various realistic scenarios for glacial erosion. This is necessary to get simulations with no, or negligible, glacial erosion over e.g. the last 15 glacial cycles, while at the same time covering scenarios that combine low subaerial erosion, limited burial under ice, and negligible glacial erosion over all glacials, except the last two glacial periods. We thus separate the probability distributions for the glacial erosion into three categories, i.e. the last glaciation (ε_{MIS2}), the penultimate glaciation (ε_{MIS6}), and all earlier glaciations during the Quaternary (ε_{Early}). Note that the duration of the last glaciation is by no means limited to marine isotope stage (MIS) 2, but is determined solely by the δ^{18}O-threshold value, as is the case for all ice-covered periods. We then limit the maximum possible amount of erosion for each glacial period to 2 m, as removal of a rock layer of this thickness is often considered sufficient to remove TCNs produced during previous periods of exposure (Gosse and Phillips, 2001; Larsen et al., 2014). The full range of Monte Carlo model simulations carried out in this study is designed to integrate

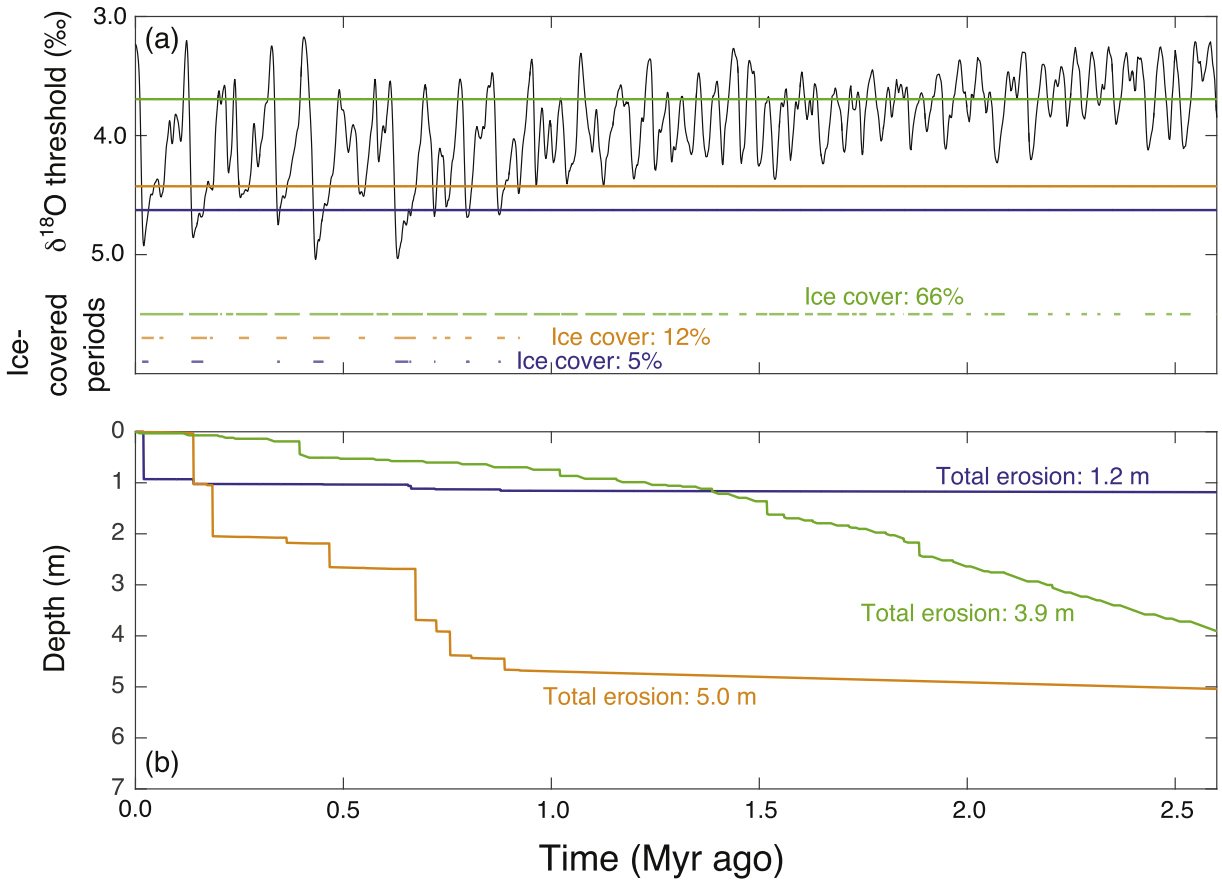

Fig. 3. (a) Three examples of how a δ^{18}O-threshold value is applied to the marine benthic δ^{18}O record of Lisiecki and Raymo (2005) in order to define the ice-cover histories in the Monte Carlo simulations. The ice-cover histories associated with the three δ^{18}O-threshold values (3.69‰ (green), 4.43‰ (magenta), and 4.63‰ (blue)) are shown by the dotted lines in the bottom of panel a. (b) Exhumation histories associated with the three different ice covers in the bottom of panel a. Apart from the δ^{18}O-threshold values, each of the three exhumation histories are defined by a random subaerial erosion rate and an independent stochastic erosion events associated with each ice-covered period. (For interpretation of the references to colour in this figure legend, the reader is referred to the Web version of this article.)

different probability distributions in order to thoroughly explore the model space, and thus include a total of 8×10^6 simulations that are combined into one pool (Table 1). For instance, the 2×10^6 simulations carried out with setup #2 (Table 1) ensures that we include scenarios resembling burial under cold-based non-erosive ice, characterized in the model simulations by low or negligible erosion during all glacial periods (less than 0.1 m of glacial erosion despite burial under ice during 99% of the Quaternary). It is important to note, however, that by assigning a discrete amount of erosion to each ice-covered period, independently of the erosion during other ice-covered periods, it is not possible to determine the most likely exposure/burial and erosion history associated with a given set of ^{10}Be and ^{26}Al concentrations. The model simulations only allow us to explore the range of possible exposure/burial and erosion histories for a given set of concentrations. Interpreting the most likely exposure/burial and erosion history should therefore involve comparison to other ^{26}Al/^{10}Be data from nearby locations and integration of field observations and geological/geomorphological constraints.

For each simulation, the model combines a δ^{18}O-threshold value with a constant interglacial erosion rate and a range of independent glacial erosion values, which makes it possible to calculate the change in ^{10}Be and ^{26}Al concentrations over time as the simulated sample moves towards the surface due to erosion (Fig. 3). Importantly, as starting concentration, we use the secular equilibrium concentration calculated using the subaerial erosion rate also used for ice-free conditions during the Quaternary, as determined by the δ^{18}O-threshold value. Note that the secular equilibrium concentration is calculated for the depth where the sample was at the onset of the Quaternary 2.6 Myr ago. Hence, for a sample that experienced 5.0 m of total erosion during the Quaternary, the initial nuclide concentrations were calculated for a sample buried under 5.0 m of bedrock, which leads to starting concentrations at the onset of the Quaternary that plot deep inside the standard two-isotope diagram (Fig. 4). Trajectories evolving from their starting points track changes in ^{26}Al/^{10}Be vs. ^{10}Be, driven by production during ice-free periods and loss due to radioactive decay, over the

Table 1
Compilation of the four model setups designed to combine a wide range of exposure/burial histories, subaerial erosion rates, and, in particular, glacial erosion histories. N refers to the number of model simulations carried out with each setup, while δ^{18}O is the range of δ^{18}O-threshold values, and ε_{int} the range of subaerial erosion rates used for the pre-Quaternary and during ice-free periods in the Quaternary. $\varepsilon_{MIS2\ and\ }\varepsilon_{MIS6}$ refer to the range of glacial erosion during the last and penultimtae glacial periods, whereas ε_{Early} is the range of glacial erosion in all earlier glacial periods.

	N	δ^{18}O	ε_{no_ice}	ε_{MIS2}	ε_{MIS6}	ε_{Early}
#1	2×10^6	3.25–4.85	0.05–50	0-2 m	0-2 m	0-2 m
#2	2×10^6	3.25–4.85	0.05–50	0–0.2 m	0–0.2 m	0–0.2 m
#3	2×10^6	3.25–4.85	0.05–50	0-2 m	0–0.2 m	0–0.2 m
#4	2×10^6	3.25–4.85	0.05–50	0-1 m	0-1 m	0–0.2 m

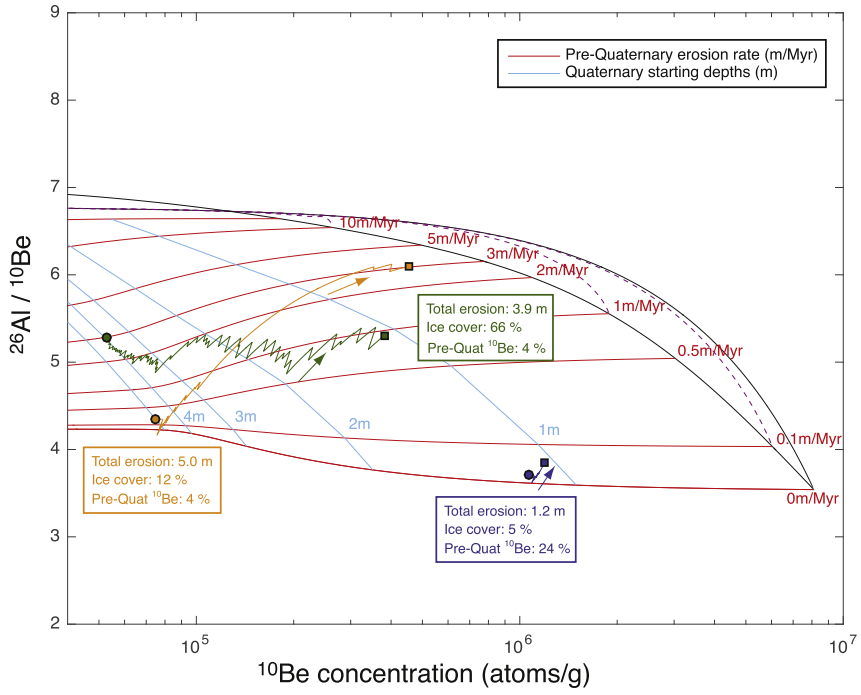

Fig. 4. Two-isotope burial plot showing the $^{26}Al/^{10}Be$ vs. ^{10}Be trajectories associated with the three exhumation and ice-cover histories outlined in Fig. 3. The red and cyan iso-lines show how the $^{26}Al/^{10}Be$ ratios and ^{10}Be concentrations develop from the onset of the Quaternary (coloured circles) towards the present (coloured squares) and are therefore not decay-corrected. The $^{26}Al/^{10}Be$ ratios and concentrations at the onset of the Quaternary depend on the pre-Quaternary erosion rate (red) and the depth under the surface 2.6 Myr ago (cyan), which is equal to the amount of total erosion during the Quaternary. The term "Total erosion" refers to the total amount of subaerial and glacial erosion a sample has experienced during the Quaternary, while "Ice cover" refers to the total amount of burial under ice during the Quaternary. The term "Pre-Quat ^{10}Be" refers to the percentage that the decay-corrected ^{10}Be concentration at the onset of the Quaternary (coloured circles) contributes to the present ^{10}Be concentration (coloured squares). (For interpretation of the references to colour in this figure legend, the reader is referred to the Web version of this article.)

last 2.6 Myr towards the present (Fig. 4).

In this study, we investigate systematically how these trajectory end-points are related to specific exposure/burial and erosion landscape histories. To illustrate the results, we use a range of synthetic ^{10}Be and ^{26}Al sample concentrations and identify the exposure/burial and erosion histories leading to concentrations that match these concentrations within the assigned uncertainties ($\sigma_{Be} = 5\%$ and $\sigma_{Al} = 5\%$). In the simulations, the depth-dependent production rates are calculated as the sum of production due to neutron spallation, negative muons, and fast muons. For simplicity, we adopt the following parameters directly from Margreth et al. (2016): a reference ^{10}Be production rate for neutron spallation of 4.0 atoms/(g*yr) (Borchers et al., 2016), a reference $^{26}Al/^{10}Be$ production ratio of 6.75 (Balco et al., 2008), reference ^{10}Be and ^{26}Al production rates for negative muons of 0.06 atoms/(g*yr) and 0.49 atoms/(g*yr) (Lifton et al., 2014; Heisinger et al., 2002a,b), respectively, and reference ^{10}Be and ^{26}Al production rates for fast muons of 0.02 atoms/(g*yr) and 0.16 atoms/(g*yr) (Lifton et al., 2014; Heisinger et al., 2002a,b), respectively. Furthermore, we use ^{10}Be and ^{26}Al half-lives of 1.378 Myr (Chmeleff et al., 2010) and 720 kyr (Nishiizumi, 2004), respectively, and attenuation lengths for neutron spallation, negative and fast muons of 150 g/cm^2 (Balco et al., 2008; Gosse and Plillips, 2001), 1500 g/cm^2 (Heisinger et al., 2002a,b; Braucher et al., 2011), and 4320 g/cm^2 (Heisinger et al., 2002b; Braucher et al., 2011), respectively. Finally, we apply a rock density of 2.65 g/cm^3. Recent studies suggest that the $^{26}Al/^{10}Be$ production ratio may be higher than the commonly used reference value of 6.75, at least in the Arctic (Argento et al., 2013; Corbett et al., 2017). To explore the importance of this aspect, we repeated the simulations described above, using the $^{26}Al/^{10}Be$ production ratio of 7.3 reported in a recent study of continuously exposed bedrock and boulder surfaces in Greenland (Corbett et al., 2017).

3. Results

The new approach in this study, which attempts to fully integrate Quaternary erosion histories, including both variable and low constant erosion rates, provides a novel perspective on how ^{26}Al and ^{10}Be concentrations may evolve over time. Importantly, the removal of overlying rock due to Quaternary erosion implies that ^{10}Be and ^{26}Al concentrations initially evolve from a point inside the $^{26}Al/^{10}Be$ vs. ^{10}Be diagram, and not from the constant erosion envelope (Fig. 4). A starting point at the constant erosion envelope would require that the sample has remained at the surface (no erosion during the Quaternary) or, alternatively, that the initial concentrations are negligible compared to those accumulated throughout the Quaternary. The latter assumption may not be fulfilled for landforms that were covered by ice for extensive periods and experienced low pre-Quaternary erosion rates and limited total erosion during the Quaternary. However, the contribution of the nuclides inherited from the pre-Quaternary decreases with increasing pre-Quaternary erosion rates, increasing amounts of total erosion during the Quaternary, and decreasing burial under Pleistocene ice covers (Fig. 5). Not surprisingly, lower pre-Quaternary erosion rates are associated with lower $^{26}Al/^{10}Be$ ratios at the starting point, simply because ^{26}Al decays almost twice as fast as ^{10}Be and lower erosion rates imply more time for decay. The starting point of the Quaternary TCN trajectory can be located anywhere inside the burial plot, although only above the $^{26}Al/^{10}Be$

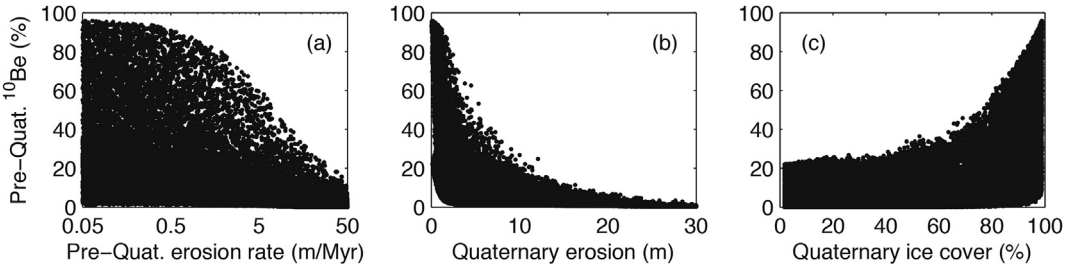

Fig. 5. Contribution of decay-corrected ^{10}Be concentrations at the onset of the Quaternary to the present concentration of ^{10}Be as a function of (a) pre-Quaternary erosion rates, (b) total amount of erosion during the Quaternary, and (c) total amount of burial under ice during the Quaternary. The panels show 5×10^4 randomly selected model simulations out of a total of 8×10^6 simulations.

equilibrium line for zero erosion (lowermost red line in Fig. 4). The starting point is displaced increasingly leftwards (towards lower ^{10}Be concentrations) for increasing amounts of Quaternary erosion (cyan lines in Fig. 4) and upwards (towards higher ^{26}Al/^{10}Be ratios) for increasing erosion rates during the pre-Quaternary (red lines in Fig. 4).

The shape and length of the TCN trajectory depend on the Quaternary exposure history, but also on when and how quickly the sample was brought to the surface by erosion. Importantly, the TCN trajectory cannot reach the constant erosion envelope of the ^{26}Al/^{10}Be vs. ^{10}Be diagram if slow non-glacial erosion and full surface exposure continue to dominate throughout most of the Quaternary (e.g. in the form of transport-limited subaerial weathering), and is supplemented by a few efficient erosion events during the most recent 2–3 glaciations (dark blue trajectory in Fig. 4). Essentially, there is not enough time to increase the ^{26}Al/^{10}Be ratio to levels near the constant erosion envelope following the most recent glaciations, because the time spent in the high-production zone near the surface is too short. A sample that experienced such a scenario (Fig. 7 a–c) would, according to the standard interpretation of the ^{26}Al/^{10}Be vs. ^{10}Be burial plot, imply prolonged burial by non-erosive ice, when in fact the burial time was limited and the ice was erosive.

The fact that the starting point of the Quaternary TCN trajectory can be located deep inside the two-isotope diagram because the initial exposure to cosmic rays is occurring at depth, implies that vastly different exposure/burial histories can lead to the same TCN concentrations for some areas of the burial plot (Fig. 6). It is nevertheless possible to infer some general trends concerning the solution loci that satisfy given combinations of ^{10}Be and ^{26}Al. The total Quaternary erosion is low and very well constrained for low ^{26}Al/^{10}Be ratios (<4.5), in particular for high ^{10}Be concentrations plotting close to the constant erosion envelope (Fig. 6). Not surprisingly, the amount of total erosion tends to increase with decreasing ^{10}Be concentration and increasing ^{26}Al/^{10}Be ratios. For high ^{26}Al/^{10}Be ratios (>5.5), however, the total erosion during the Quaternary is poorly defined, except for high ^{10}Be concentrations (^{10}Be > 2×10^6 atoms/g) that plot close to the constant erosion envelope. In contrast, the duration of burial under ice is rarely uniquely defined, as the range of possible ice-cover fractions is wide for most ^{26}Al/^{10}Be ratios (Fig. 5). However, low ^{26}Al/^{10}Be ratios (<4.5) combined with low ^{10}Be concentrations (<~2×10^5 atoms/g) are uniquely associated with prolonged burial under ice. Conversely, low ^{26}Al/^{10}Be ratios (<4.5) combined with high ^{10}Be concentrations (>2×10^6 atoms/g) are only compatible with very limited burial under ice. The erosion associated with samples plotting in this area of the burial field mainly takes place during the most recent glacial periods, in particular MIS2-4 and MIS6.

The model simulations thus show that very high degrees of Pleistocene exposure (>80%) combined with low subaerial erosion rates and significant glacial erosion (>1 m) during the most recent glacial maxima can result in low ^{26}Al/^{10}Be ratios (e.g. Fig. 7 a–c). Conversely, high ^{26}Al/^{10}Be ratios are not necessarily associated with limited ice covers, but may in fact be associated with prolonged burial under ice. A rather extreme example of such a scenario is given in Fig. 7 d–f, in which the total amount of exposure throughout the Quaternary is 7%, but because the sample was briefly exposed during the most recent interglacials, while being located close to the surface, the ^{26}Al/^{10}Be ratio increase to >6 towards the present. The overall pattern of results is robust against changes in the ^{26}Al/^{10}Be production ratio. Changing the ^{26}Al/^{10}Be production ratio from 6.75 to 7.3 does not influence the overall pattern, but it does shift the various combinations of ^{26}Al/^{10}Be vs. ^{10}Be (i.e. synthetic samples in Fig. 6) so that their relationship with, or distance to, the constant erosion envelope remains unchanged (see Supplementary Fig. 1). For instance, more burial under ice is required to get very low ^{26}Al/^{10}Be ratios (~3.5) for a^{26}Al/^{10}Be production rate of 7.3 compared to a production rate of 6.75.

4. Discussion

The systematic exploration of how different exposure/burial histories lead to different or, in some cases, similar ^{26}Al/^{10}Be ratios and absolute concentrations, has some fundamental implications for the interpretation of existing paired ^{26}Al/^{10}Be bedrock data. Our results thus map out how a range of different exposure/burial and erosion histories may lead to the same ^{26}Al/^{10}Be ratio, highlighting that paired ^{26}Al/^{10}Be data often cannot be uniquely associated with one particular exposure/burial history, as noted in earlier studies (e.g. Gosse & Phillips, 2001). However, the simulations also offer a possibility to reconcile spatially-varying ^{26}Al/^{10}Be data, in particular from locations where relatively uniform, long-term ice-cover histories would be expected, such as homogeneous high-elevation plateaus or neighbouring alpine summits.

4.1. Simulating the ice-cover and erosion history of the alpine summits of northwestern Svalbard

The steep alpine summits in northwestern Svalbard, which stand several hundred meters above the surrounding glaciers, experienced very limited subaerial and/or glacial erosion over the last several hundred thousand years (Gjermundsen et al., 2015). Low ^{26}Al/^{10}Be ratios in 8 out of 10 samples from 8 individual peaks have been interpreted to indicate that these summits were shielded by glacial ice throughout the last 0.78–1.24 Myr or more (Fig. 8). Nevertheless, two samples taken a few meters apart from the alpine summit of “Kongen” yield very different ^{26}Al/^{10}Be ratios (6.2 and 3.4, respectively). The high ^{26}Al/^{10}Be ratio of 6.2 is suggested to

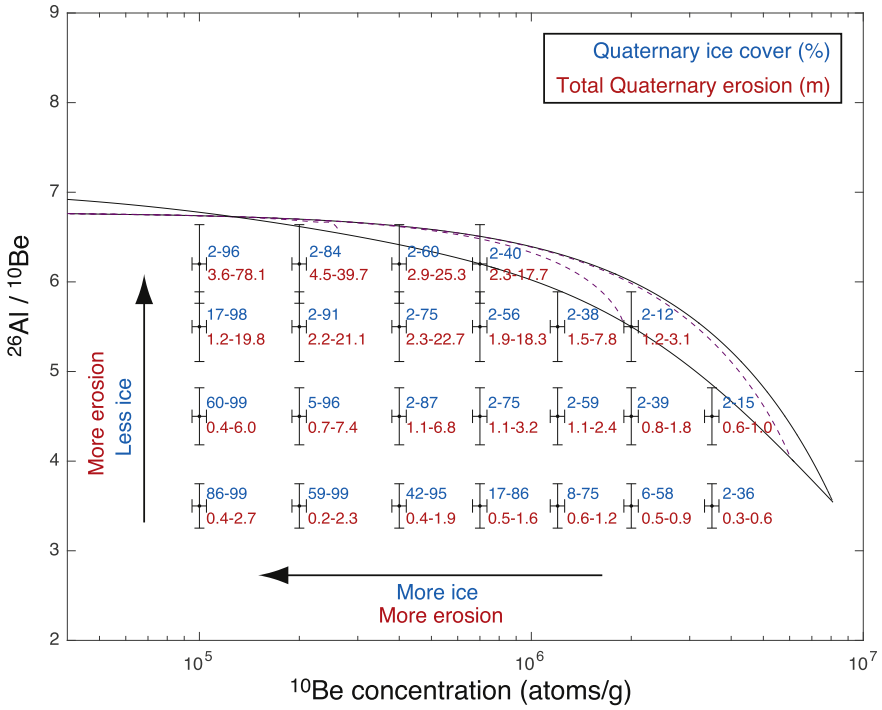

Fig. 6. The range of total ice-cover fractions during the Quaternary (blue) and total amounts of erosion during the Quaternary (red) of the model simulations that fit specific points, or synthetic test samples, in the ^{26}Al/^{10}Be vs ^{10}Be diagram within errors. The associated error bars are based on a 5% uncertainty of the ^{10}Be and ^{26}Al concentrations. The red and blue numbers are based on 8×10^6 numerical simulations combining a wide range of different exposure/burial and erosion histories. The subaerial erosion rate, which is applied to the pre-Quaternary as well as ice-free periods during the Quaternary, was randomly selected from the range 0.05 m/Myr – 50 m/Myr in each simulation. The glacial erosion is simulated as distinct erosion events that are independent of glacial erosion during other ice-covered periods. The glacial erosion associated with each glacial period is limited to the range 0–2 m. (For interpretation of the references to colour in this figure legend, the reader is referred to the Web version of this article.)

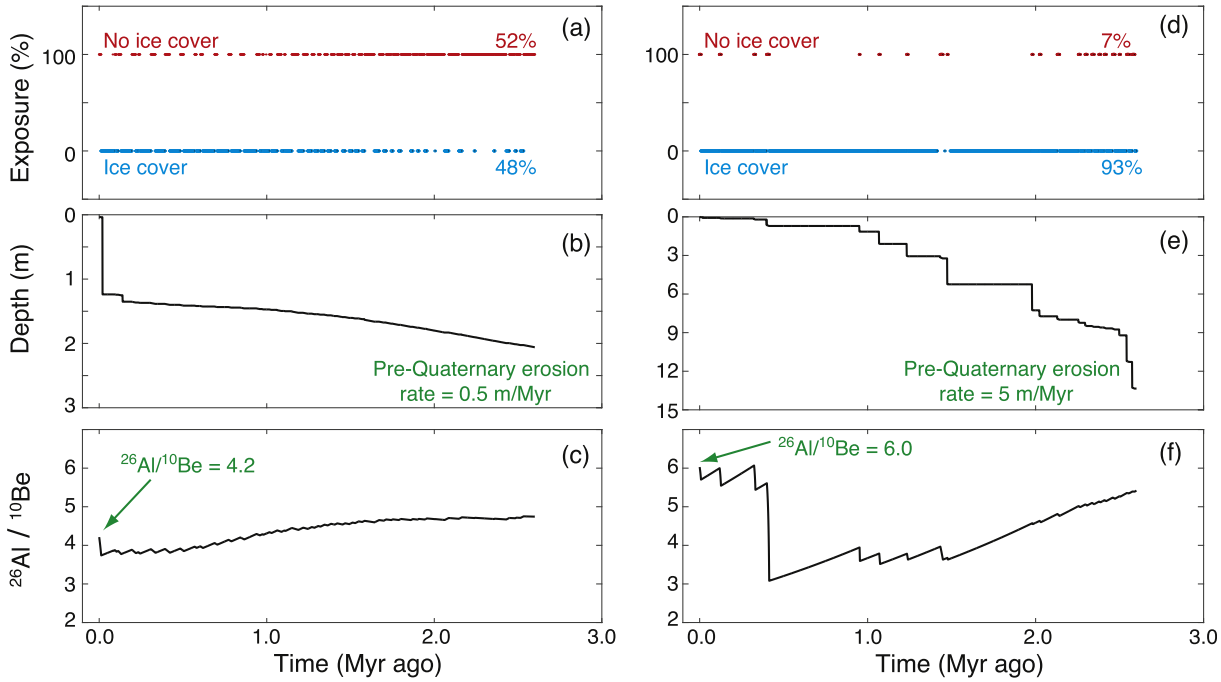

Fig. 7. Two landscape evolution scenarios demonstrating that low and high ^{26}Al/^{10}Be ratios not necessarily reflect prolonged burial under ice and limited burial under ice, respectively. Panels on the left describe (a) the exposure/burial history, (b) exhumation history, and (c) the associated evolution of the ^{26}Al/^{10}Be ratio for a scenario with significant exposure during the Quaternary (52%) combined with significant erosion during the last glacial period, for instance via glacial plucking. Panels on the right describe (d) the exposure/burial history, (e) exhumation history, and (f) the associated evolution of the ^{26}Al/^{10}Be ratio for a scenario with a rather extreme degree of burial under ice during the Quaternary and a transition from burial under erosive ice to burial under non-erosive ice at some point during the mid-Pleistocene.

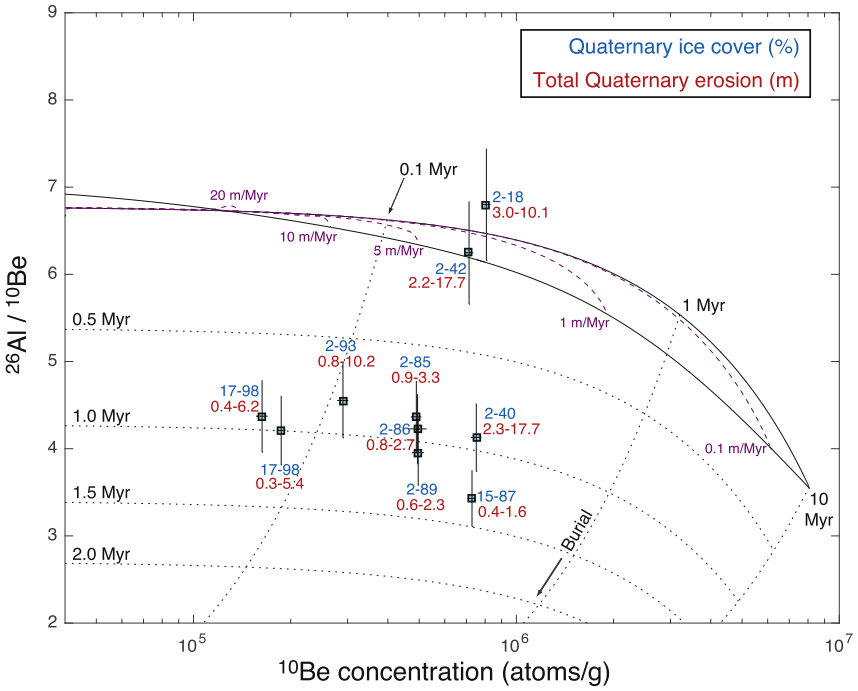

Fig. 8. Paired ^{26}Al and ^{10}Be data from the steep alpine summits of northwestern Svalbard (Gjermundsen et al., 2015). All concentrations are normalized to sea-level. The numbers in blue next to the Svalbard samples (cyan squares) show the total Quaternary ice-cover fractions of the simulations that match the ^{26}Al and ^{10}Be concentrations from Svalbard within the error bars. The numbers in red show the total amount of erosion during the Quaternary that match the ^{26}Al and ^{10}Be concentrations within error bars. For all samples, we used total uncertainties of 5% and 8% for ^{10}Be and ^{26}Al, respectively. (For interpretation of the references to colour in this figure legend, the reader is referred to the Web version of this article.)

result from a rock fall during the mid-Quaternary, but our simulations indicate that such a high ratio combined with high absolute concentrations are incompatible with continuous ice cover throughout the last 1 Myr (Fig. 8). On the contrary, our simulations indicate that both these samples can be explained by burial under ice during 15–40% of the Quaternary (using total uncertainties of $\sigma_{Be} = 5\%$ and $\sigma_{Al} = 8\%$), although with different amounts of total erosion (Fig. 9). In the overlapping interval, characterized by an ice cover of 15–40%, the sample with a ^{26}Al/^{10}Be ratio of 3.4 experienced a total erosion of 1.3–1.6 m where the sample with a ratio of 6.2 experienced a total erosion of 2.4–15.0 m (Fig. 9b). A notable difference between models satisfying the ^{26}Al/^{10}Be data from these two samples is that the erosion during the last two glacial periods was negligible for the high-ratio sample (^{26}Al/^{10}Be = 6.2). In contrast, most of the erosion associated with the low-ratio sample (^{26}Al/^{10}Be = 3.4) took place during the last two glacial periods, for example as glacial plucking of the steep bedrock ridges or as rock falls in response to ice loading/unloading. The occurrence of such rock falls is not unlikely given the steep nature of the summits (Gjermundsen et al., 2015). The simulations furthermore suggest that the subaerial erosion rate during the Quaternary, as well as the pre-Quaternary, must have been very low, i.e. < 3 m/Myr for the high-ratio sample (^{26}Al/^{10}Be = 6.2) and ~1 m/Myr or less for the low-ratio sample (^{26}Al/^{10}Be = 3,4), respectively. To our knowledge, there are no geological constraints that preclude such limited subaerial erosion rate of these summits during the Quaternary or pre-Quaternary. In fact, subaerial erosion rates around 1 m/Myr or less are needed to explain the combination of a high ^{10}Be

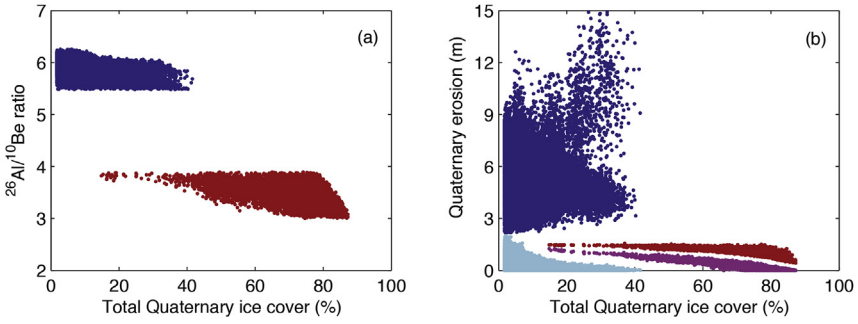

Fig. 9. Model simulations that fit the ^{10}Be and ^{26}Al data from the two samples taken a few meters apart from the steep summit of "Kongen", northwestern Svalbard. (a) Total ice cover during the Quaternary for the simulations that fit the concentrations of the sample with a ^{26}Al/^{10}Be ratio of 3.4 (red dots) and a ratio of 6.2 (blue dots), respectively. (b) Erosion during the Quaternary as a function of the total Quaternary ice cover for the simulations that fit the ^{26}Al/^{10}Be data. Red (^{26}Al/^{10}Be = 3.4) and blue (^{26}Al/^{10}Be = 6.2) dots denote the total erosion during the Quaternary for the two samples, whereas the magenta (^{26}Al/^{10}Be = 3.4) and cyan (^{26}Al/^{10}Be = 6.2) dots denote the erosion associated with the last glacial period. Note how the total erosion during the Quaternary is dominated by erosion associated with the last glacial period for simulations with relatively low ice covers fitting the sample with ^{26}Al/^{10}Be = 3.4. (For interpretation of the references to colour in this figure legend, the reader is referred to the Web version of this article.)

concentration and a low $^{26}Al/^{10}Be$ ratio measured in one of the samples from the summit of "Kongen". This is also the case when using the two-stage minimum-limiting exposure and burial model to interpret the data.

Our simulations show that prolonged burial under minimally erosive ice throughout the last 1 Myr, albeit with a total exposure of ~5% distributed over the warmest interglacial periods is indeed possible for the 8 samples characterized by $^{26}Al/^{10}Be$ ratios <5, which is in agreement with the interpretation of Gjermundsen et al. (2015). However, the model simulations also show that all 10 $^{26}Al/^{10}Be$ datasets can be explained by exposure/burial histories that include burial under ice for as little as 17% of the last 2.6 Myr (40% of the last 1 Myr) (Fig. 8), roughly corresponding to ice cover during Marine Isotope Stages (MIS) 2–4 over the last glacial cycle. The only exception is a sample from a summit close to the coast ($^{26}Al/^{10}Be$ ratio = 6.8), which, according to our results, must have experienced burial under ice less than 20% of the Quaternary period (Fig. 8). The range of total erosion during the Quaternary vary from 0.4 to 1.6 m ($^{26}Al/^{10}Be = 3.4$) to 3.0–17.7 m ($^{26}Al/^{10}Be = 6.2$), with the majority of samples requiring a total amount of within the range 0.5–5.0 m. Our model simulations of the combined data from Svalbard therefore suggest that these steep summits could have remained ice free throughout large parts of the Pleistocene, and that the summits possibly only were covered by ice during the coldest parts of the glacial periods. In fact, this is the most straightforward interpretation if we impose the geological constraint that the ice cover must have been more-or-less similar for the various summits, as well as for the two samples from the summit of "Kongen". This scenario, however, contrasts with the interpretation of Gjermundsen et al. (2015), who infer more or less continuous ice cover throughout the last 1 Myr.

4.2. General implications for the interpretation of Quaternary ice covers and erosion rates

Our simulations demonstrate how widely different exposure/burial and erosion histories can lead to similar ^{10}Be and ^{26}Al concentrations, and that low $^{26}Al/^{10}Be$ ratios are not uniquely associated with prolonged burial under ice as was the case for the Svalbard samples Conversely, high $^{26}Al/^{10}Be$ ratios combined with relatively low absolute concentrations do not necessarily reflect insignificant burial under ice, but may in fact be associated with prolonged ice covers throughout large parts of the Quaternary. For instance, an area that was buried under erosive ice throughout the early-middle part of the Quaternary, during which it experienced significant erosion (>3 m), and subsequently experienced a transition to burial under non-erosive ice, punctured only by brief periods of exposure during the warmest interglacials, may quite easily reach $^{26}Al/^{10}Be$ ratios >6 (e.g. Fig. 7 d–f). The key aspect of this scenario is that the sample is brought close to the surface at some point before the most recent interglacial periods, and that the absolute concentrations are sufficiently low for the subsequent exposure to drive up the $^{26}Al/^{10}Be$ ratio. The model simulations thus offer new possibilities for reconciling spatially-varying $^{26}Al/^{10}Be$ data from mapped high-elevation surfaces, such as those found in western Greenland, the Torngat Mountains, on Baffin Island, and elsewhere. This is particularly relevant at locations where geological or geomorphological considerations or other field constraints suggest that the ice-sheet history was relatively homogeneous and coherent within a certain area. In such cases, a sample displaying a high $^{26}Al/^{10}Be$ ratio and high absolute concentrations may be used to infer a limited degree of burial under ice across the area in question, as suggested above for the alpine summits of northwestern Svalbard. Alternatively, a sample characterized by a low $^{26}Al/^{10}Be$ ratio and low absolution concentrations can be used to infer prolonged burial under ice across a wider area.

4.3. The influence of pre-Quaternary erosion rates

To decipher the most likely exposure/burial and erosion history from inverse modelling of $^{26}Al/^{10}Be$ data, it is essential to use the available field observations and geological/geomorphological constraints to guide the modelling and subsequent interpretation. Such constraints may include the presence of weathering pits, grussy weathered surfaces, regolith, blockfields, and freshly eroded glacial erratics. Importantly, if credible estimates of the pre-Quaternary erosion rate are available for the specific site in question, this information should be integrated in the model setup as the pre-Quaternary erosion rate along with the subaerial erosion rate during the Quaternary may limit the range of possible exposure/burial and erosion histories that fit the measured $^{26}Al/^{10}Be$ data. To investigate this aspect, we carried out additional simulations, using the setup and parameter values in Table 1 with the only exception that the subaerial erosion rate (ε_{no_ice}) was held constant at 1, 5, 10, and 20 m/Myr, respectively. The simulations show that as the pre-Quaternary erosion rate, along with the subaerial erosion rate during the Quaternary, increase, more burial under ice is required to explain low $^{26}Al/^{10}Be$ ratios (Fig. 10). In general, the range of possible exposure/burial scenarios, as well as the amount of total erosion during the Quaternary, becomes increasingly limited as the pre-Quaternary rate increases. For low $^{26}Al/^{10}Be$ ratios, the total amount of erosion during the Quaternary tends to decrease with increasing pre-Quaternary erosion rates, but this relationship also depends on the absolute concentrations. A more notable effect, however, is that an increasingly smaller portion of the $^{26}Al/^{10}Be$ data in the two-isotope diagram can be accounted for as the pre-Quaternary erosion rate increases (Fig. 10), simply because higher subaerial erosion rates are incompatible with high concentrations of ^{10}Be and ^{26}Al. This implies that for a significant fraction of the $^{26}Al/^{10}Be$ data in the literature, such as those from northwestern Svalbard, the subaerial erosion rate must be very low (<5 m/Myr, and in some cases < 1 m/Myr). Another possibility is that the subaerial erosion rates changed significantly over time, or, alternatively, that production rate was higher than suggested by the available scaling models.

By combining geological constraints with detailed inverse modelling of the $^{26}Al/^{10}Be$ data, it may be possible to determine if the long-term ice cover in the circum-Arctic regions really was quite limited as suggested by some studies (e.g. Beel et al., 2016), or, alternatively, much more continuous and prolonged as suggested by other studies (e.g. Corbett et al., 2013; Gjermundsen et al., 2015). While there clearly may be local and regional differences in the long-term ice cover in the Arctic, our simulations suggest that it is also a distinct possibility that the spatially-varying $^{26}Al/^{10}Be$ data to a large degree reflect spatial differences in the erosion history, including the timing of the erosion. It is thus possible that the Pleistocene ice-cover was much more limited than hitherto believed at many high-elevation surfaces in western Greenland and Arctic Canada. The opposite, however, is also a distinct possibility, in which case the spatially-varying $^{26}Al/^{10}Be$ data primarily reflect variable degrees of glacial erosion during the mid-Quaternary.

5. Conclusions

In this study, we have used a new Monte Carlo model approach to investigate systematically the combined effects of variable erosion rates, including the timing of erosion, and the exposure/burial history associated with Pleistocene ice covers on concentrations of ^{10}Be and ^{26}Al in surface samples. The model simulations

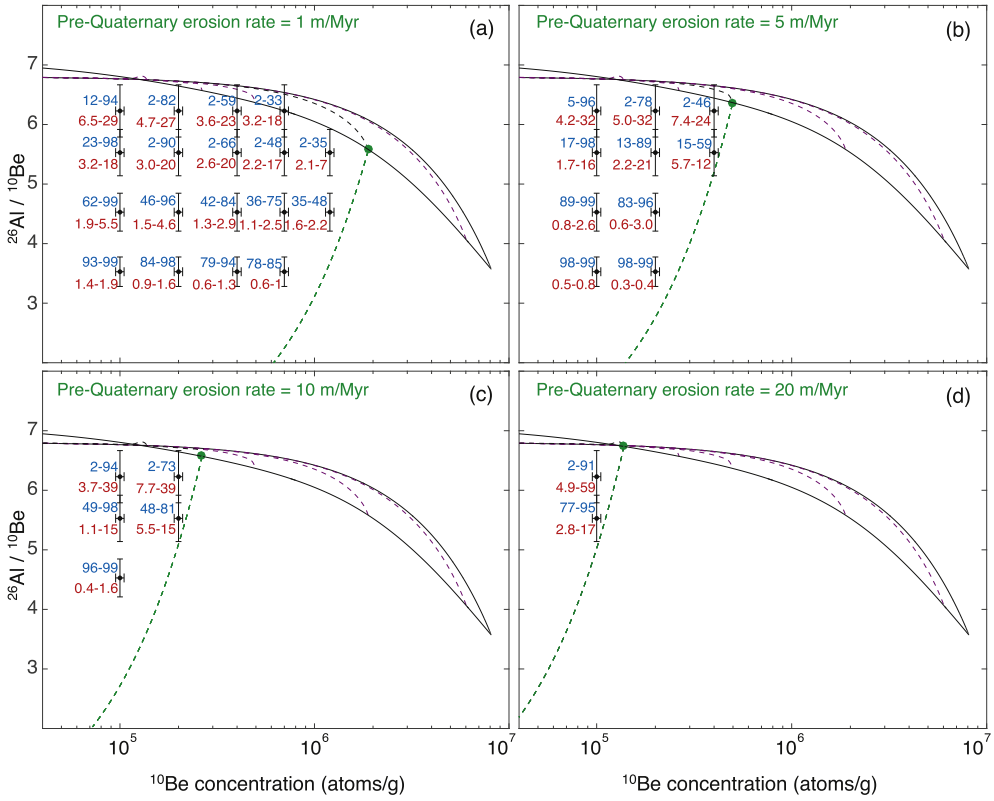

Fig. 10. The range of total ice-cover fractions during the Quaternary (blue) and total amounts of erosion during the Quaternary (red) of the model simulations that fit specific points, or synthetic test samples, in the $^{26}Al/^{10}Be$ vs ^{10}Be diagram within errors. The associated error bars are based on a 5% uncertainty of the ^{10}Be and ^{26}Al concentrations. The numbers are based on model simulations carried out with the setup described in Table 1, and outlined in Fig. 6, with the only exception that the subaerial erosion rate during the pre-Quaternary, as well as the Quaternary, was held constant at (a) 1 m/Myr, (b) 5 m/Myr, (c) 10 m/Myr, and (d) 20 m/Myr, respectively. The green dots denote the secular equilibrium $^{26}Al/^{10}Be$ ratios and ^{10}Be concentrations for subaerial erosion rates of (a) 1 m/Myr, (b) 5 m/Myr, (c) 10 m/Myr, and (d) 20 m/Myr. The dashed green lines denote the change in $^{26}Al/^{10}Be$ vs ^{10}Be associated with radioactive decay under ice-covered conditions (i.e. no exposure). (For interpretation of the references to colour in this figure legend, the reader is referred to the Web version of this article.)

show that low $^{26}Al/^{10}Be$ ratios do not necessarily reflect prolonged burial under ice, but may as well reflect very limited burial under ice combined with abrupt exhumation within the last glacial cycles, e.g. due to glacial plucking. Similarly, high $^{26}Al/^{10}Be$ ratios may also reflect a wide range of exposure/burial histories, including prolonged burial under ice combined with a transition from erosive to non-erosive glacial regimes during the mid-Pleistocene. The absolute concentrations of ^{10}Be and ^{26}Al, along with geological/geomorphological constraints that may guide the modelling and interpretation, are thus key to determining the most likely erosion and exposure/burial history experienced by a sample. Based on the model simulations, we propose that a large part of the spatially-varying $^{26}Al/^{10}Be$ data from bedrock surfaces in the circum-Arctic regions experienced similar long-term burial under ice, but varying amounts of glacial erosion.

Acknowledgements

Mads Faurschou Knudsen is grateful for financial support from the Villum Foundation (VKR023114), whereas David Egholm acknowledges financial support from the Danish Council for Independent Research Natural Sciences (DFF-6108-00226).

Appendix A. Supplementary data

Supplementary data related to this article can be found at https://doi.org/10.1016/j.quascirev.2017.12.012.

References

Anderson, R.S., Anderson, S.P., 2010. Geomorphology - the Mechanics and Chemistry of Landscapes. Cambridge University Press, 651 pp.
Argento, D., Reedy, R., Stone, J., 2013. Modeling the Earth's cosmic radiation. Nucl. Instrum. Meth. Phys. Res. B 294, 464–469.
Argento, D., Stone, J., Reedy, R., O'Brien, O., 2015a. Physics-based modeling of cosmogenic nuclides part I - Radiation transport methods and new insights. Quat. Geochronol. 26, 29–43.
Argento, D., Stone, J., Reedy, R., O'Brien, O., 2015b. Physics-based modeling of cosmogenic nuclides part II – key aspects of in-situ cosmogenic nuclide production. Quat. Geochronol. 26, 44–55.
Balco, G., Stone, J.O., Lifton, N.A., Dunai, T.J., 2008. A complete and easily accessible means of calculating surface exposure ages or erosion rates from ^{10}Be and ^{10}Al measurements. Quat. Geochronol. 3, 174–195.
Beel, C.R., Lifton, N.A., Briner, J.P., Goehring, B.M., 2016. Quaternary evolution and ice sheet history of contrasting landscapes in Uummannaq and Sukkertoppen, western Greenland. Quat. Sci. Rev. 248–258.
Bierman, P.R., Marsella, K.A., Patterson, C., Davis, P.T., Caffee, M., 1999. Mid-Pleistocene cosmogenic minimum-age limits for pre-Wisconsinan glacial surfaces in southwestern Minnesota and southern Baffin Island: a multiple nuclide approach. Geomorphology 27, 25–39.
Bierman, P.R., Shakun, J.D., Corbett, L.B., Zimmerman, S.R., Rood, D.H., 2016. A persistent and dynamic East Greeland Ice Sheet over the past 7.5 million years. Nature 540, 256–260.
Blard, P.-H., Leduc, G., 2016. Cosmic signature. Nature 540, 202–203.
Borchers, B., Marrero, S., Balco, G., Caffee, M., Goehring, B., Lifton, N., Nishiizumi, K., Phillips, F., Schaefer, J., Stone, J., 2016. Geological calibration of spallation production rates in the CRONUS-Earth project. Quat. Geochronol. 31, 188–198.
Braucher, R., Merchel, S., Borgomano, J., Bourlès, D.L., 2011. Production of cosmogenic radionuclides at great depth: a multi element approach. Earth Planet Sci. Lett. 309, 1–9.
Briner, J.P., Miller, G.H., Thompson Davis, P., Finkel, R.C., 2006. Cosmogenic radionuclides from fiord landscapes support differential erosion by overriding ice sheets. Bull. Geol. Soc. Am. 118, 406–420.
Briner, J.P., Lifton, N.A., Miller, G.H., Refsnider, K., Anderson, R., Finkel, R.C., 2014.

Using in situ cosmogenic ^{10}Be, ^{14}C, and ^{26}Al to decipher the history of polythermal ice sheets on Baffin Island, Arctic Canada. Quat. Geochronol. 19, 4–13.
Chmeleff, J., von Blanckenburg, F., Kossert, K., Jakob, D., 2010. Determination of the ^{10}Be half-life by multicollector ICP-MS and liquid scintillation counting. Nucl. Instrum. Methods Phys. Res. Sect. B Beam Interact. Mater. Atoms 268, 192–199.
Shakun, J.D., Marcott, S.A., Mix, A.C., Eby, M., Kulp, S., Leverman, A., Milne, G.A., Pfister, P.L., Santer, B.D., Schrag, D.P., Solomon, S., Stocker, T.F., Strauss, B.H., Weaver, A.J., Winkelmann, R., Archer, D., Bard, E., Goldner, A., Lambeck, K., Pierrehumbert, R.T., Plattner, G.-K., 2016. Consequences of twenty-first-century policy for multi-millennial climate and sea-level change. Nat. Clim. Change 6, 360–369.
Corbett, L.B., Bierman, P.R., Graly, J.A., Neumann, T.A., Rood, D.H., 2013. Constraining landscape history and glacial erosivity using paired cosmogenic nuclides in Upernavik, Northwest Greenland. Bull. Geol. Soc. Am. 125, 1539–1553.
Corbett, L.B., Bierman, P.R., Rood, D.H., Caffee, M.W., Lifton, N.A., Woodruff, T.E., 2017. Cosmogenic ^{26}Al/^{10}Be surface production ratio in Greenland. Geophys. Res. Lett. 44, 1350–1359.
Fabel, D., Stroeven, A.P., Harbor, J., Kleman, J., Elmore, D., Fink, D., 2002. Earth Planet. Sci. Lett. 201, 397–406.
Gibbons, A.B., Megeath, J.D., Pierce, K.L., 1984. Probability of moraine survival in a succession of glacial advances. Geology 12, 327–330.
Gjermundsen, E.F., Briner, J.P., Akcar, N., Foros, J., Kubik, P.W., Salvigsen, O., Hormes, A., 2015. Minimal erosion of Arctic alpine topography during late Quaternary glaciation. Nat. Geosci. 8, 789–792.
Glasser, N., 2016. Glaciological puzzle. Nature 540, 203.
Gosse, J.C., Plillips, F.M., 2001. Terrestrial in situ cosmogenic nuclides: theory and application. Quat. Sci. Rev. 20, 1475–1560.
Granger, D., 2006. A review of burial dating methods using ^{26}Al and ^{10}Be. Geol. Soc. Am. Spec. Pap. 415, 1–16.
Heisinger, B., Lal, D., Jull, A., Kubik, P., Ivy-Ochs, S., Neumaier, S., Knie, K., Lazarev, V., Nolte, E., 2002a. Production of selected cosmogenic radionuclides by muons: 1. Fast muons. Earth Planet. Sci. Lett. 200, 345–355.
Heisinger, B., Lal, D., Jull, A., Kubik, P., Ivy-Ochs, S., Knie, K., Nolte, E., 2002b. Production of selected cosmogenic radionuclides by muons: 2. Capture of negative muons. Earth Planet. Sci. Lett. 200, 357–369.
Kessler, M.A., Anderson, R.S., Briner, J.P., 2008. Fjord insertion into continental margins driven by topographic steering of ice. Nat. Geosci. 1, 365–369.
Klein, J., Giegengack, R., Middleton, R., Sharma, P., Underwood, J.R., Weeks, R.A., 1986. Revealing histories of exposure using in situ produced 26Al and 10Be in Libyan Desert Glass. Radiocarbon 28, 547–555.
Kleman, J., Lundqvist, J., Stroeven, A.P., 2008. Patterns of quaternary ice sheet erosion and deposition in Fennoscandia. Geomorphology 97, 73–90.
Knudsen, M.F., Egholm, D.L., Jacobsen, B.H., Larsen, N.K., Jansen, J.D., Andersen, J.L., Linge, H.C., 2015. A multi-nuclide approach to constrain landscape evolution and past erosion rates in previously glaciated terrains. Quat. Geochronol 30, 100–113.
Lambeck, K., Rouby, H., Purcell, A., Sun, Y., Sambridge, M., 2014. Sea level and global ice volumes from the last glacial maximum to the holocene. Proc. Natl. Acad. Sci. U. S. A. 111, 15296–15303.
Lane, T.P., Roberts, D.H., Rea, B.R., Cofaigh, C.O., Vieli, A., Rhodés, A., 2014. Controls upon the last glacial maximum deglaciation of the northern Uummannaq ice stream system, west Greenland. Quat. Sci. Rev. 92, 324–344.
Larsen, N.K., Funder, S., Kjær, K.H., Kjeldsen, K.K., Knudsen, M.F., Linge, H.C., 2014. Rapid early Holocene ice retreat in West Greenland. Quat. Sci. Rev. 92, 310–323.
Lifton, N., Sato, T., Dunai, T.J., 2014. Scaling in situ cosmogenic nuclide production rates using analytical approximations to atmospheric cosmic-ray fluxes. Earth Planet. Sci. Lett. 386, 149–160.
Lisiecki, L.E., Raymo, M.E., 2005. A Pliocene-Pleistocene stack of 57 globally distributed benthic δ^{18}O records. Paleoceanography 20, 1–17.
Margreth, A., Gosse, J.C., Dyke, A.S., 2016. Quantification of subaerial and episodic subglacial erosion rates on high latitude upland plateaus: cumberland Peninsula, Baffin Island, Arctic Canada. Quat. Sci. Rev. 133, 108–129.
Nielsen, T., Kuijpers, A., 2013. Only 5 southern Greenland shelf edge glaciations since the early Pliocene. Sci. Rep. 3, 1875.
Nishiizumi, K., Winterer, E.L., Kohl, C.P., Klein, J., Middleton, R., Lal, D., Arnold, J.R., 1989. Cosmic ray production rates of ^{10}Be and ^{26}Al in quartz from glacially polished rocks. J. Geophys. Res. Solid Earth 94, 17907–17915.
Nishiizumi, K., Kohl, C.P., Arnold, J.R., Klein, J., Fink, D., Middleton, R., 1991. Cosmic ray produced 10Be and 26Al in Antarctic rocks: exposure and erosion history. Earth Planet. Sci. Lett. 104, 440–454.
Nishiizumi, K., 2004. Preparation of 26Al AMS standards. Nucl. Instrumen. Methods Phys. Res. Sect. B Beam Interact. Mater. Atoms 223–224, 388–392.
Roberts, D.H., Long, A.J., Schnabel, C., Davies, B.J., Xu, S., Simpson, M.J.R., Huybrechts, P., 2009. Ice sheet extent and early deglacial history of the southwestern sector of the Greenland Ice Sheet. Quat. Sci. Rev. 28, 2760–2773.
Roberts, D.H., Rea, B.R., Lane, T.P., Schnabel, C., Rodés, A., 2013. New constraints on Greenland ice sheet dynamics during the last glacial cycle: evidence from the Uummannaq ice stream system. J. Geophys. Res. Earth Surf. 118, 519–541.
Schaefer, J.M., Finkel, R.C., Balco, G., Alley, R.B., Caffee, M.W., Briner, J.P., Young, N.E., Gow, A.J., Schwarz, R., 2016. Greenland was nearly ice-free for extended periods during the Pleistocene. Nature 540, 252–255.
Small, E.E., Anderson, R.S., Repka, J.L., Finkel, R., 1997. Erosion rates of alpine bedrock summit surfaces deduced from in situ 10Be and 26Al. Earth Planet. Sci. Lett. 150, 413–425.
Staiger, J.K.W., Gosse, J.C., Johnson, J.V., Fastook, J., Gray, J.T., Stockli, D.F., Stockli, L., Finkel, R., 2005. Quaternary reflief generation by polythermal glacier ice. EarthSurf. Process. Landforms 30, 1145–1159.
Strunk, A., Knudsen, M.F., Egholm, D.L., Jansen, J.D., Levy, L.B., Jacobsen, B.H., Larsen, N.K., 2017. One million years of glaciation and denudation history in west Greenland. Nat. Comm. 8 (14999), 1–8.
Sugden, D.E., 1974. Landscapes of glacial erosion in Greenland and their relationship to ice, topographic and bedrock conditions. Inst. Br. Geogr. Spec. Publ. 7, 177–195.
Sugden, D.E., John, B.S., 1976. Glaciers and Landscape: a Geomorphological Approach (Edward Arnold, London).